Supplementary Information

for

Manipulating the Raman Scattering Rotation via Magnetic Field in MoS_2 Monolayer

Yi Wan,[a, b, †, *] Xing Cheng,[b, c,†] Yanfang Li,[d] Yaqian Wang,[d] Yongping Du,[a] Yibin Zhao,[a] Bo Peng,[d] Lun Dai[b, c, *] and Erjun Kan[a, *]

[a] Department of Applied Physics and Institution of Energy and Microstructure, Nanjing University of Science and Technology, Nanjing 210094, China

[b] State Key Laboratory for Artificial Microstructure & Mesoscopic Physics, School of Physics, Peking University, Beijing 100871, China

[c] Collaborative Innovation Center of Quantum Matter, Beijing 100871, China

[d] National Engineering Research Center of Electromagnetic Radiation Control Materials and State Key Laboratory of Electronic Thin Films and Integrated Devices, School of Microelectronics and Solid State Electronics, University of Electronic Science and Technology of China, Chengdu 610054, China

[†] These authors contributed equally to this work.

[*] Correspondence and requests for materials should be addressed to

Y. W. (email: wany@njust.edu.cn)

L. D. (email: lundai@pku.edu.cn)

E. J. K. (email: ekan@njust.edu.cn)

S1. The average value of lateral dimension of MoS_2 triangles.

S2. PL and Raman spectroscopy mapping.

S3. Polarization-resolved Raman spectra measurement for MoS_2 samples with different crystal orientations.

S4. Polarization-resolved Raman spectra of monolayer MoS_2 at selected magnetic fields.

S5. Influences of Landau levels.

S6. Faraday rotation and systematic error.

S7. Magneto-PL measurement set-up.

S8. The selection of the excitation wavelengths for Raman and PL spectra.

S9. Excitonic transitions and Zeeman shifts in MoS_2 monolayer.

1. The average value of lateral dimension of MoS_2 triangles.

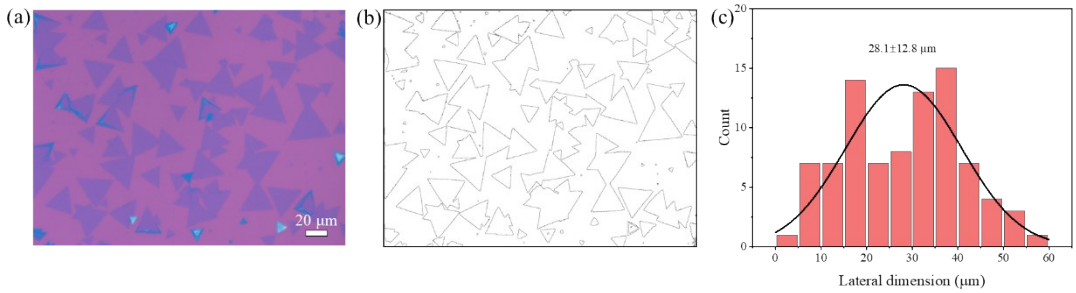

Figure S1. (a) Optical microscopy image of MoS_2 flakes grown on Si/SiO_2. (b) The line profiles for MoS_2 triangles are extracted from the optical microscopy image (a), obtained by Image J software. (c) Statistical (including at least 80 triangles) lateral dimensions for the CVD-synthesized MoS_2 samples; the corresponding average value of the triangular edge length is around 28.1±12.8 μm.

MoS_2 samples were synthesized directly on the surface of Si/SiO_2 substrates via the commonly-used chemical vapor deposition (CVD) method. From the optical microscopy image (Figure S1 (a)), we can see most MoS_2 domains on Si/SiO_2 appear as triangles, obeying the symmetry of the hexagonal crystal lattice. We further performed the statistical calculations about the lateral dimension of MoS_2 triangles, with assistance of Image J software (Figure S1 (b)). The average value of lateral dimension (viz, the side length) of the MoS_2 triangles is around 28.1±12.8 μm (Figure S1 (c)).

2. PL and Raman spectroscopy mapping.

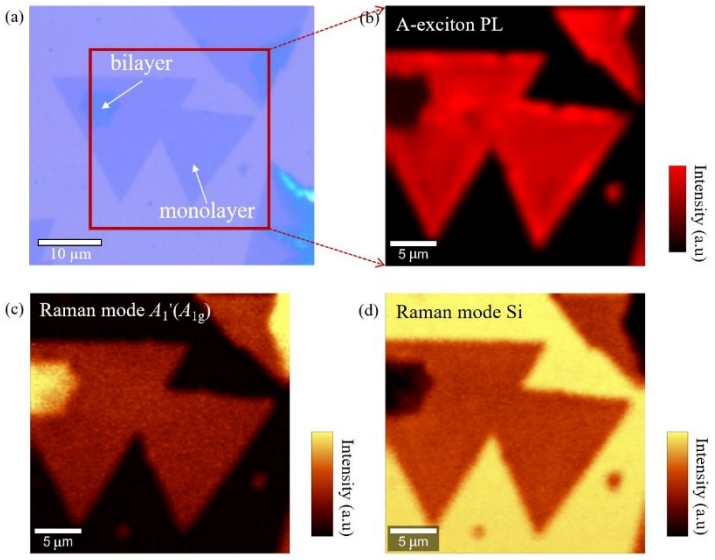

Figure S2. (a) Optical microscopy image of a MoS_2 sample with monolayer and bilayer domains. The square marked is chosen for PL and Raman spectroscopy collection. (b) PL mapping of MoS_2 A-exciton. (c, d) Raman spectroscopy mapping of (c) MoS_2 $A_1'(A_{1g})$ mode and (d) Si peak.

We prepared mono- and bi-layer MoS_2 samples by using a CVD method. Typical triangular samples are with the lateral dimension ranging from 10 to 50 μm. The statistical average value of lateral dimension (viz, the side length) of the MoS_2 triangles is around 28.1±12.8 μm. We identified the area with thin MoS_2 samples with an optical microscope by optical contrast (Figure S2 (a)). Both PL (Figure S2 (b)) and Raman (Figure S2 (c, d)) spectroscopy mapping images were collected to estimate the sample quality. For PL studies, MoS_2 monolayers were excited with a 532 nm laser. The PL in bilayer MoS_2, which is an indirect-gap semiconductor, is a phonon-assisted luminescence process with negligible PL intensities compared with the monolayer MoS_2. We attribute the uniform photoluminescence of MoS_2 monolayers to direct-gap luminescence, demonstrating the high quality of the monolayer samples. Generally speaking, the intensity of Raman signals is in direct proportion to the sample contents. Therefore, the intensity of *A*-mode from the bilayer is stronger than that from the monolayer. Besides, due to the screening effect, the Si peak located at 521 cm^{-1} from the bare Si/SiO_2 substrate is clearer than the area covered by MoS_2 samples.

3. Polarization-resolved Raman spectra measurement for MoS_2 samples with different crystal orientations.

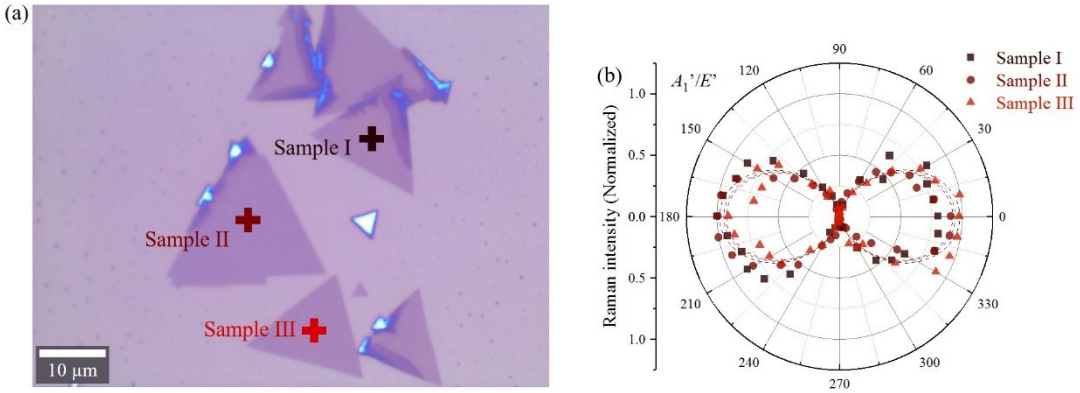

Figure S3. (a) Optical microscopy image of the discrete monolayer MoS_2 triangles on Si/SiO_2. Three MoS_2 samples with different crystal lattice orientations, are chosen for polarization-resolved Raman spectra measurement and labelled as Sample I, II and III. (b) Polar plots of the ratio of A_1' mode integrated intensities to that of E' mode as a function of the polarization angles between the incident and scattered lights, collected from the three samples as shown in (a).

For some certain anisotropic materials, such as 1T'-$MoTe_2$ and T_d-WTe_2, the in-plane Raman signal patterns remarkedly depend on the relationship between the scattered light polarization angle and the material crystalline *a*-axis. However, this situation does not exist for isotropic monolayer 1H-MoS_2. To prove this, we chose some discrete monolayer MoS_2 triangular domains with different crystalline orientations, randomly grown on Si/SiO_2 (Figure S3 (a)). As we can see from the polar plots of the integrated intensity ratio of A_1'/E' (Figure S3 (b)), all the polar plots depict a two-lobe shape, and the main-axes are parallel to the 0^o-180^o direction, regardless of the MoS_2 crystalline orientation, only dependent on the polarization angles between the incident and scattered lights.

4. Polarization-resolved Raman spectra of monolayer MoS_2 at selected magnetic fields.

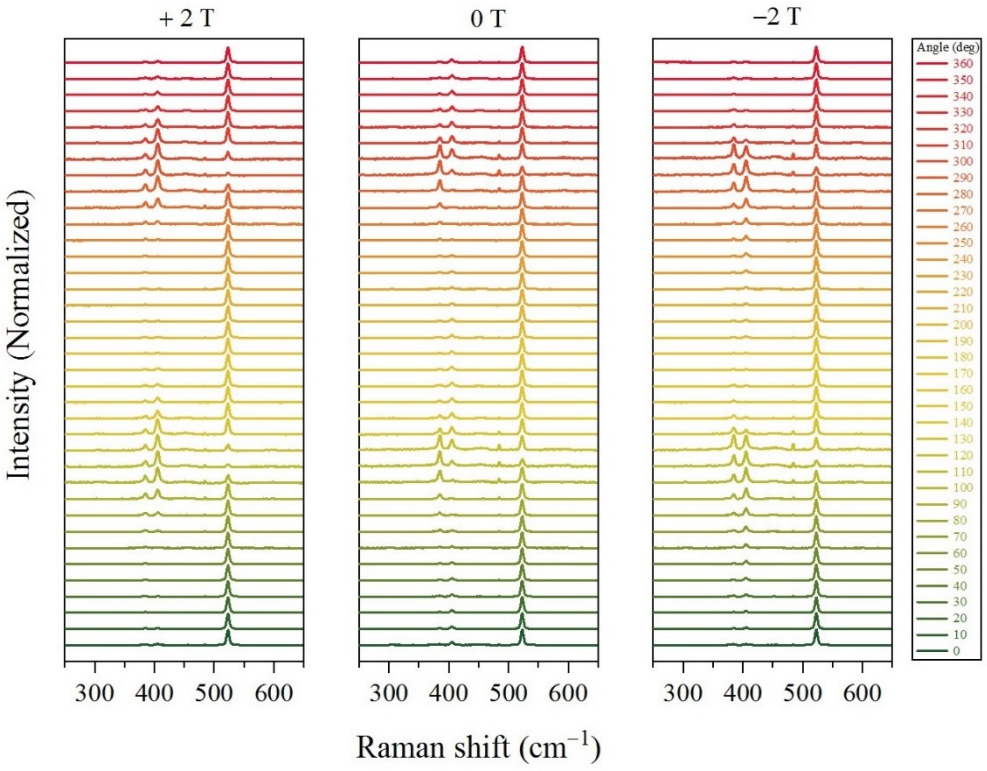

Figure S4. Raman spectra of the as-grown MoS_2 monolayers versus the polarization angles between the incident and scattered lights, measured at +2 T (left panel), 0 T (middle panel) and -2 T (right panel).

Figure S4 provides a series of polarization-resolved Raman spectra of MoS_2 monolayer at some representative magnetic fields (0, ± 2 T). These Raman spectra were collected by rotating the analyzer before the spectrometer, viz, by changing the polarization angle between the incident and scattered lights. We took 10^0 as the step. The polarization angles have already been listed on the right panel. As we can see, there are three dominant peaks located at 384, 404 and 521 cm^{-1}, correspond to the MoS_2 *E*', *A*' mode and Si substrate. All the Raman spectra were normalized by the peak with the highest intensity.

5. Influences of Landau levels.

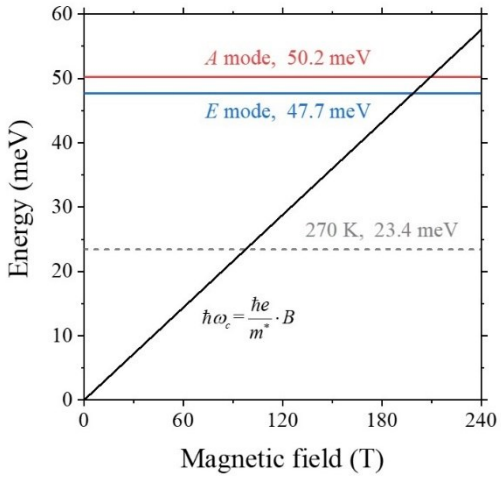

Figure S5. Comparison of Landau levels, thermal energy (270 K) and phonon frequencies for *A*- and *E*-mode for MoS_2 monolayer under magnetic fields.

If the magnetic field reaches very high, the influence of Landau levels (LLs, $\hbar w_c = \hbar eB/m^*$) will become non-neglected. Generally, the emergence of LLs under magnetic fields will subtly modify the original band structures and perhaps remarkably affect the optical transitions, which may result in a Raman resonance if the allowed optical transition energetically matches LLs.

Our measurements were performed at 270 K and at a relatively small magnetic field (±5 T), at which the transitions between LLs ($\hbar w_c$) are completely smeared out (Ming-Che Chang and Qian Niu, *Phys. Rev. B.*, **1996**, 53(11), 7010-7023; E. A. Fajardo and R. Winkler, *Phys. Rev. B.*, **2019**, 100(12), 125301), as shown in Figure S5. The LLs interaction must be taken into consideration at very low temperatures or very high magnetic field, and the experimental observations may be significantly different from those in our current results.

6. Faraday rotation and systematic error.

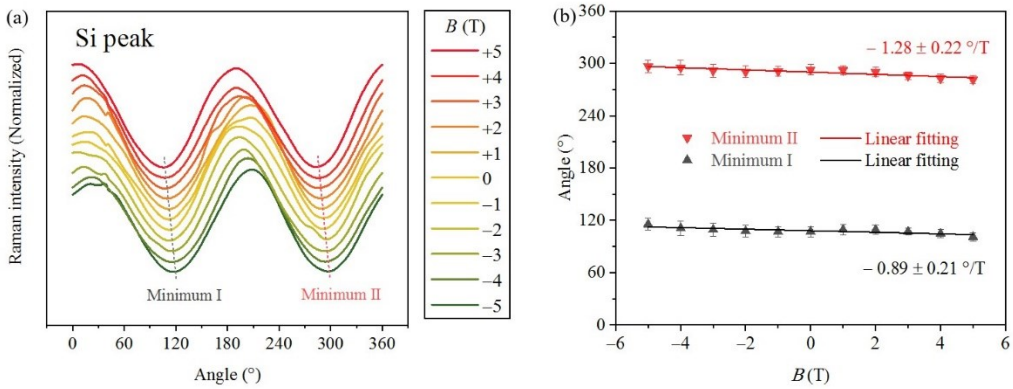

Figure S6. (a) Intensity of Si peak located at around 521 cm^{-1} as a function of the polarization angles between the incident and scattered lights, collected from the Si/SiO_2 substrate. As the magnetic field changes, there exhibits a slight monotonic trend in a series of polarization-resolved micro-zone Raman spectra, especially for the angle where the minimum of Si Raman peak locates, perhaps contributed from the Faraday effect. (b) The angles where the minimum locates versus the magnetic field. The fitting linear slopes of -1.28±0.22 and -0.89±0.21^{o}/T are obtained, corresponding to the two minimums as shown in (a), respectively.

Besides the giant magneto-optical Raman effect in MoS_2 *A'* mode, we also observe a tiny twofold symmetry axis rotation phenomenon in the Si peak located at 521 cm^{-1}. As the magnetic field changes, there exhibits a slight monotonic trend in the series of polarization-resolved micro-zone Raman spectra (Figure S6 (a)). The effective fitting linear slope of -1.09^{o}/T is obtained (Figure S6 (b)). We attribute the shift in the twofold-axis of symmetry to the Faraday effect, or known as Faraday rotation. According to the definition in physics, Faraday effect or Faraday rotation mainly describes a magneto-optical phenomenon in which a rotation takes place in the polarization plane of an electromagnetic wave in existence of a magnetic field that is applied along the beam propagation direction. The amplitude of the polarization plane rotation is proportional to the magnetic field component along the light beam direction.

7. Magneto-PL measurement set-up.

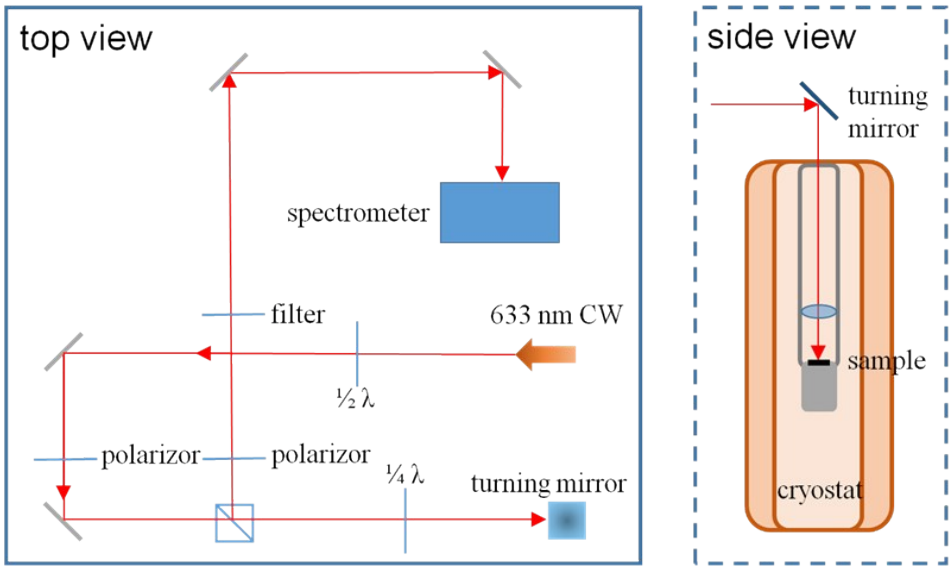

Figure S7. Schematic diagram of the experimental set-up for the magneto-PL measurements. Positive magnetic field is defined as the upward direction. The left- and right- circularly polarized components of the light emitting from the sample are analyzed by a combination of a linear polarizer and a quarter wave plate (¼ λ).

8. The selection of the excitation wavelengths for Raman and PL spectra.

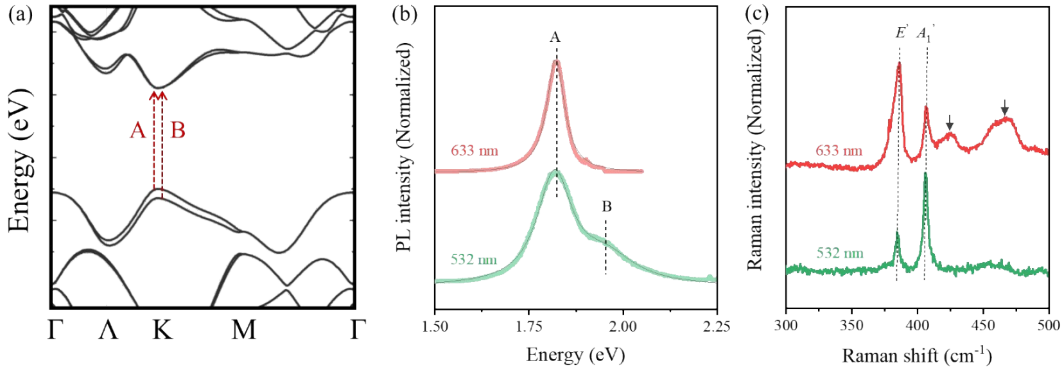

Figure S8. (a) Calculated band structure of monolayer MoS_2. The direct excitonic transitions (A and B, indicated by red dashed arrows) occur at K point. The splitting in valence band maxima arises form spin-orbit coupling. (b) PL spectra obtained from monolayer MoS_2, excited by 633 nm and 532 nm lasers, respectively. (c) Raman spectra obtained from monolayer MoS_2, excited by 633 nm and 532 nm lasers, respectively.

The selection of the excitation wavelengths for Raman and PL spectra is very important. Figure S8 (a) provides the calculated energy band structure of monolayer MoS_2. At

K(K') valleys in momentum space, the highest-energy valence bands and the lowest-energy conduction bands are mainly of molybdenum *d*-orbital character. Because of the broken inversion symmetry, spin-orbit interactions split the valence bands by ~160 meV, inducing two direct excitonic transitions marked by A (E_A~1.82 eV) and B (E_B ~1.98 eV) excitons, respectively. Thus, if we pump the MoS_2 monolayers by a laser with the excitation energy between E_A and E_B, for example, 633 nm (1.96 eV), only signals from A excitons will be captured (red curve, Figure S8 (b)). For comparison, if we pump the MoS_2 monolayers by a laser with the excitation energy higher than E_B, for example, 532 nm (2.33 eV), signals from A and B excitons will be both captured (green curve, Figure S8 (b)). Besides, previous literature (Kin Fai Mak, et al, *Nat. Nanotechnol.*, **2012**, 7, 494-498) claims that, to obtain the polarization-resolved PL spectrum, the excitation on resonance with the A exciton is necessary. This behavior is understood to be a consequence of the relaxation of the optical selection rules: off-resonance excitation simultaneously populates both K and K' valleys, generating no net polarization. As a result, we chose 633 nm (1.96 eV) laser for polarization-resolved PL spectra excitation on resonance with the A exciton. Accordingly, 594 nm (2.09 eV) lasers are more suitable for the excitation on resonance with the B exciton.

Then, Figure S8 (c) displays the Raman spectra of monolayer MoS_2 excited by 633 nm and 532 nm. The signals of *E*' and A_1' modes excited by 633 nm and 532 nm are obvious. However, in obvious contrast, the Raman spectra excited by 633 nm have more Raman peaks, e. g., a Raman-inactive mode due to a two-phonon scattering process involving a longitudinal quasi-acoustic phonon and a transverse optical phonon, B_{1u}, and a second-order zone-edge phonon peak, 2LA(M), as marked by black arrows (red curve, Figure S8 (c)), which is owing to the resonance Raman scattering, because the 633 nm excitation is in resonance with the direct band gap (A exciton) at the K point (Hong Li, et al, *Adv. Funct. Mater.*, **2012**, 22, 1385-1390). Since we mainly focus on these two Raman features, *E*' and A_1', for convenience of data analysis, we chose 532 nm laser for Raman spectra excitation.

9. Excitonic transitions and Zeeman shifts in MoS_2 monolayer.

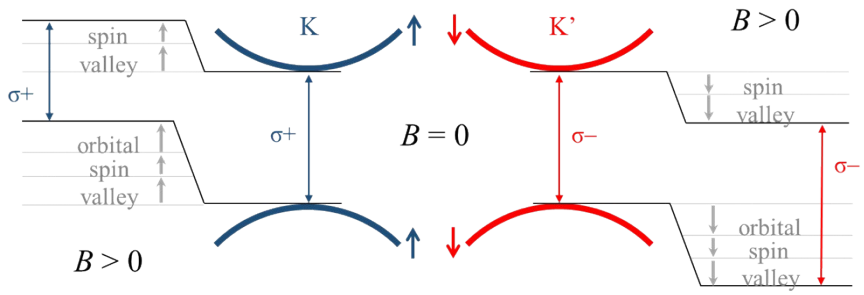

Figure S9. Valley Zeeman effect in existence of *B*//*c*-axis. The degeneracy of K and K' valleys is lifted resulted from the total contributions from the spin magnetic moment μ_s, the valley magnetic moment μ_k, and the atomic orbital magnetic moment μ_l. The signs of these three contributions are opposite in the two sets of degenerate-but-inequivalent valleys. The spin contribution to Zeeman valley shift (Δ) is estimated to be zero, because the optically-allowed excitonic transitions require both conduction and valence bands to possess the same spin.

Origin for Zeeman splitting in MoS_2 monolayers can be understood by studying the contribution of valley, spin and atomic orbital magnetic moments to the electronic energy levels at K and K' valley. Given the time-reversal symmetry at B=0 T, the energies of electrons are intrinsically degenerate, at K and K' valleys. Under a perpendicular magnetic field (B), this degeneracy is broken, resulting in an energy difference between the two valleys by the Zeeman effect.

For K or K' valleys in MoS_2 monolayers, the excitonic Zeeman shift can be expressed as $-(\mu^c-\mu^v)\cdot B$, where $\mu^c(\mu^v)$ represents the total magnetic moment in the conduction (valence) band. For a given electronic state at K or K' valley, the μ^c and μ^v contain the spin, the atomic orbital, and the valley orbital magnetic moments, represented as μ_s, μ_l, and μ_k, respectively. The contribution from spin magnetic moment to the excitonic Zeeman shift is estimated to be zero because the optically-allowed excitonic transitions require the electrons in both of conduction and valence bands to possess the same spin, whereas the conduction and valence bands comprise of different atomic orbits. For conduction bands, azimuthal orbital angular momentum l_z=0 (μ_l^c=0) is associated with the d_{z^2} orbits. For valence bands, the hybridized $d_{x^2-y^2}\pm id_{xy}$ orbitals cause $l_z=\pm 2\hbar$ ($\mu_l^v=\pm 2\mu_B$) at K and K' valleys, respectively, where μ_B means the Bohr magneton. This difference is estimated to induce a Zeeman shift of $\mp 2\mu_B\cdot B$ for K and K' excitons, respectively, resulting in an exciton Zeeman splitting of $-4\mu_B\cdot B$ (corresponding to a g

factor of 4). Concerning the valley magnetic moments, at the conduction and valence band electronic states $\mu_k^c=\pm(m_0/m_e^*)\mu_B$ and $\mu_k^v=\pm(m_0/m_h^*)\mu_B$ at K and K' valleys, respectively. In a general model where $m_e^*\neq m_h^*$, the valley orbital contributions will result in a divergence of the excitonic Zeeman splitting, slightly away from $-4\mu_B \cdot B$.